Research Article

Giuliana Galati*, Andrey Alexandrov, Behcet Alpat, Giovanni Ambrosi, Stefano Argirò,
Raul Arteche Diaz, Nazar Bartosik, Giuseppe Battistoni, Nicola Belcari, Elettra Bellinzona,
Silvia Biondi, Maria Giuseppina Bisogni, Graziano Bruni, Pietro Carra, Piergiorgio Cerello,
Esther Ciarrocchi, Alberto Clozza, Sofia Colombi, Alberto Del Guerra, Micol De Simoni,
Antonia Di Crescenzo, Benedetto Di Ruzza, Marco Donetti, Yunsheng Dong, Marco Durante,
Riccardo Faccini, Veronica Ferrero, Emanuele Fiandrini, Christian Finck, Elisa Fiorina,
Marta Fischetti, Marco Francesconi, Matteo Franchini, Gaia Franciosini, Luca Galli,
Valerio Gentile, Giuseppe Giraudo, Ronja Hetzel, Enzo Iarocci, Maria Ionica, Antonio Iuliano,
Keida Kanxheri, Aafke Christine Kraan, Valeria Lante, Chiara La Tessa, Martina Laurenza,
Adele Lauria, Ernesto Lopez Torres, Michela Marafini, Cristian Massimi, Ilaria Mattei,
Alberto Mengarelli, Andrea Moggi, Maria Cristina Montesi, Maria Cristina Morone,
Matteo Morrocchi, Silvia Muraro, Federica Murtas, Alessandra Pastore, Nadia Pastrone,
Vincenzo Patera, Francesco Pennazio, Pisana Placidi, Marco Pullia, Fabrizio Raffaelli,
Luciano Ramello, Riccardo Ridolfi, Valeria Rosso, Claudio Sanelli, Alessio Sarti,
Gabriella Sartorelli, Osamu Sato, Simone Savazzi, Lorenzo Scavarda, Angelo Schiavi,
Christoph Schuy, Emanuele Scifoni, Adalberto Sciubba, Alexandre Sécher, Marco Selvi,
Leonello Servoli, Gianluigi Silvestre, Mario Sitta, Roberto Spighi, Eleuterio Spiriti,
Giancarlo Sportelli, Achim Stahl, Valeri Tioukov, Sandro Tomassini, Francesco Tommasino,
Marco Toppi, Giacomo Traini, Serena Marta Valle, Marie Vanstalle, Mauro Villa, Ulrich Weber,
Roberto Zarrella, Antonio Zoccoli, and Giovanni De Lellis

Charge identification of fragments with the emulsion spectrometer of the FOOT experiment

Abstract: The FOOT (FragmentatiOn Of Target) experiment is an international project designed to carry out the fragmentation cross-sectional measurements relevant for charged particle therapy (CPT), a technique based on the use of charged particle beams for the treatment of deep-seated tumors. The FOOT detector consists of an electronic setup for the identification of $Z \geq 3$ fragments and an emulsion spectrometer for $Z \leq 3$ fragments. The first data taking was performed in 2019 at the GSI facility

* **Corresponding author: Giuliana Galati,** Department of Physics "M. Merlin", University of Bari, Bari, Italy, e-mail: giuliana.galati@uniba.it
Andrey Alexandrov: National University of Science and Technology, MISIS, RUS-119049, Moscow, Russia; Department of Physics "E. Pancini", University of Napoli, Napoli, Italy; Lebedev Physical Institute of the Russian Academy of Sciences, RUS-119991, Moscow, Russia; INFN Section of Napoli, Napoli, Italy
Behcet Alpat, Valeria Lante, Marco Pullia, Simone Savazzi: Centro Nazionale di Adroterapia Oncologica (CNAO), Pavia, Italy
Giovanni Ambrosi, Maria Ionica, Keida Kanxheri, Leonello Servoli: INFN Section of Perugia, Perugia, Italy
Stefano Argirò, Lorenzo Scavarda: Department of Physics, University of Torino, Torino, Italy; INFN Section of Torino, Torino, Italy

Nazar Bartosik, Piergiorgio Cerello, Veronica Ferrero, Elisa Fiorina, Giuseppe Giraudo, Nadia Pastrone, Francesco Pennazio: INFN Section of Torino, Torino, Italy
Giuseppe Battistoni, Ilaria Mattei, Silvia Muraro, Serena Marta Valle: INFN Section of Milano, Milano, Italy
Nicola Belcari, Maria Giuseppina Bisogni, Pietro Carra, Esther Ciarrocchi, Alberto Del Guerra, Marco Francesconi, Matteo Morrocchi, Valeria Rosso, Giancarlo Sportelli: INFN Section of Pisa, Pisa, Italy; Department of Physics, University of Pisa, Pisa, Italy
Elettra Bellinzona, Benedetto Di Ruzza, Emanuele Scifoni: Trento Institute for Fundamental Physics and Applications, Istituto Nazionale di Fisica Nucleare (TIFPA-INFN), Trento, Italy
Silvia Biondi, Matteo Franchini, Cristian Massimi, Gabriella Sartorelli, Mauro Villa, Roberto Zarrella, Antonio Zoccoli: INFN

(Darmstadt, Germany). In this study, the charge identification of fragments induced by exposing an emulsion detector, embedding a C_2H_4 target, to an oxygen ion beam of 200 MeV/n is discussed. The charge identification is based on the controlled fading of nuclear emulsions in order to extend their dynamic range in the ionization response.

Keywords: particle therapy, nuclear emulsion, fragmentation

1 Introduction

Charged particles therapy (CPT) is an established therapy for cancer treatment. The advantages of CPT are due to the energy release occurring mainly at the end of the particle's path, in the Bragg peak region, and to the

enhanced biological effectiveness of hadron beams, measured in terms of the relative biological effectiveness (RBE). The RBE value, defined as the ratio of photons to charged particles dose producing the same biological effect, is assessed to an average value of 1.1 for proton beams [1]. This value is affected by both physical (i.e. particle type, dose, linear energy transfer) and biological parameters (i.e. tissue type, cell cycle phase, oxygenation level) [2], and many recent studies highly support a comprehensive analysis to reduce uncertainties on the RBE value for the clinical practice [2–4]. Regarding physical parameters, target fragmentation plays a key role as low-energy secondary fragments contribute to increment the dose deposition in normal tissues along the entrance channel and in the region surrounding the tumor. Hence, the re-assessment of the proton RBE value

Section of Bologna, Bologna, Italy; Department of Physics and Astronomy, University of Bologna, Bologna, Italy
Graziano Bruni, Alberto Mengarelli, Marco Selvi, Roberto Spighi: INFN Section of Bologna, Bologna, Italy
Alberto Clozza, Enzo Iarocci, Martina Laurenza, Claudio Sanelli, Eleuterio Spiriti, Sandro Tomassini: INFN Laboratori Nazionali di Frascati, Frascati, Italy
Sofia Colombi, Chiara La Tessa, Francesco Tommasino: Trento Institute for Fundamental Physics and Applications, Istituto Nazionale di Fisica Nucleare (TIFPA-INFN), Trento, Italy; Department of Physics, University of Trento, Trento, Italy
Micol De Simoni, Riccardo Faccini, Gaia Franciosini: INFN Section of Roma 1, Rome, Italy; Department of Physics, University of Rome La Sapienza, Rome, Italy
Antonia Di Crescenzo, Antonio Iuliano, Adele Lauria, Giovanni De Lellis: Department of Physics "E. Pancini", University of Napoli, Napoli, Italy; INFN Section of Napoli, Napoli, Italy
Marco Donetti: Centro Nazionale di Adroterapia Oncologica (CNAO), Pavia, Italy; INFN Section of Torino, Torino, Italy
Yunsheng Dong: INFN Section of Milano, Milano, Italy; Department of Physics, University of Milano, Milano, Italy
Marco Durante: Biophysics Department, GSI Helmholtzzentrum für Schwerionenforschung, Darmstadt, Germany; Technische Universität Darmstadt Institut für Festkörperphysik, Darmstadt, Germany
Emanuele Fiandrini, Gianluigi Silvestre: INFN Section of Perugia, Perugia, Italy; Department of Physics and Geology, University of Perugia, Perugia, Italy
Christian Finck, Alexandre Sécher, Marie Vanstalle: Université de Strasbourg, CNRS, IPHC UMR 7871, F-67000Strasbourg, France
Marta Fischetti, Vincenzo Patera, Angelo Schiavi: INFN Section of Roma 1, Rome, Italy; Department of Scienze di Base e Applicate per l'Ingegneria (SBAI), University of Rome La Sapienza, Rome, Italy
Luca Galli, Aafke Christine Kraan, Andrea Moggi, Fabrizio Raffaelli: INFN Section of Pisa, Pisa, Italy

Valerio Gentile: National University of Science and Technology, MISIS, RUS-119049, Moscow, Russia; INFN Section of Napoli, Napoli, Italy
Ronja Hetzel, Achim Stahl: Physics Institute III B, RWTH Aachen University, Aachen, Germany
Ernesto Lopez Torres: INFN Section of Torino, Torino, Italy; CEADEN, Centro de Aplicaciones Tecnologicas y Desarrollo Nuclear, Havana, Cuba
Michela Marafini: INFN Section of Roma 1, Rome, Italy; Museo Storico della Fisica e Centro Studi e Ricerche Enrico Fermi, Rome, Italy
Maria Cristina Montesi: Department of Chemistry, University of Napoli, Napoli, Italy; INFN Section of Napoli, Napoli, Italy
Maria Cristina Morone: Department of Physics, University of Rome Tor Vergata, Rome, Italy; INFN Section of Roma Tor Vergata, Rome, Italy
Federica Murtas: Department of Physics, University of Rome La Sapienza, Rome, Italy
Alessandra Pastore: INFN Section of Bari, Bari, Italy
Pisana Placidi: INFN Section of Perugia, Perugia, Italy; Department of Engineering, University of Perugia, Perugia, Italy
Luciano Ramello, Mario Sitta: INFN Section of Torino, Torino, Italy; Department of Science and Technological Innovation, University of Piemonte Orientale, Alessandria, Italy
Riccardo Ridolfi: Department of Physics and Astronomy, University of Bologna, Bologna, Italy
Alessio Sarti: INFN Section of Roma 1, Rome, Italy; Department of Scienze di Base e Applicate per l'Ingegneria (SBAI), University of Rome La Sapienza, Rome, Italy; Museo Storico della Fisica e Centro Studi e Ricerche Enrico Fermi, Rome, Italy
Osamu Sato: Department of Physics, Nagoya University, Nagoya, Japan
Christoph Schuy, Ulrich Weber: Biophysics Department, GSI Helmholtzzentrum für Schwerionenforschung, Darmstadt, Germany
Adalberto Sciubba, Marco Toppi: INFN Laboratori Nazionali di Frascati, Frascati, Italy; Department of Scienze di Base e Applicate per l'Ingegneria (SBAI), University of Rome La Sapienza, Rome, Italy
Valeri Tioukov: INFN Section of Napoli, Napoli, Italy
Giacomo Traini: INFN Section of Roma 1, Rome, Italy

due to secondary fragmentation is an important topic [2]. The complexity of dedicated experiments makes this milestone challenging, and in fact, very few and limited experimental data are available in the literature regarding target fragmentation, and none of them fully describes secondary fragments induced by a proton beam. The fragmentation of carbon ions (400 MeV/n) in a polycarbonate target was studied in 2011 to determine the charge-changing cross-sections by exploiting the nuclear emulsion technology [5].

In this framework, the FragmentatiOn Of Target (FOOT) experiment [6,7] has been proposed to measure the target fragmentation induced by a proton beam in the human tissues in the energy range relevant for therapeutic applications (150–250 MeV for protons and 200–400 MeV/n for carbon ions). As fragments generated by a proton beam have few micrometers range, an inverse kinematic approach has been adopted in which a beam (carbon or oxygen) impinge on targets made of carbon- and hydrogen-enriched carbon materials (C_2H_4). Therefore, the cross-section of hydrogen is derived from its linear combination.

FOOT is based on two complementary setups: a magnetic spectrometer, covering a polar angle acceptance up to about $10°$ with respect to the beam axis, for fragments $Z \geq 3$, and an emulsion spectrometer, to measure light fragments ($Z \leq 3$) up to $70°$ with respect to the beam axis.

In this article, the charge identification performance of the secondary fragments generated by the interaction of ^{16}O (200 MeV/n) beam on a C_2H_4 target by the emulsion spectrometer is reported.

The method for the charge identification is based on an established technique already performed in previous studies [8–10], consisting of a controlled fading of nuclear emulsions by means of different thermal treatments that extend the emulsion response to a broader range and make them sensitive to particles with different ionization power and charge.

2 Experimental setup and track reconstruction

In April 2019, an emulsion spectrometer was exposed to a 200 MeV/n ^{16}O ion beam at the GSI facility in Darmstadt (Germany). The spectrometer acts both as target and tracking device. The target, made of C_2H_4 layers, was embedded in the detector structure. The exposure setup also included a counter and a beam monitor in order to measure the integrated particle density and its spatial
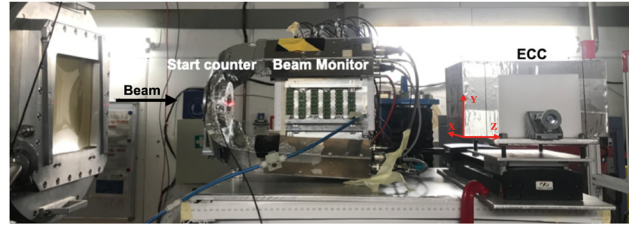

Figure 1: Experimental setup of the emulsion spectrometer used during the 2019 data taking at GSI facility.

distribution. The experimental apparatus is shown in Figure 1.

After the exposure, emulsions were first thermally treated, then developed and analyzed by fast-automated microscopes. Dedicated software algorithms were used to reconstruct tracks of impinging ions and produced fragments. In the following sections, nuclear emulsion characteristics, emulsion spectrometer exposure, structure, and the thermal treatment procedure are described.

2.1 Nuclear emulsion films

Nuclear emulsion films consist of two 70 μm thick sensitive emulsion layers, called top and bottom layers, deposited on both sides of a 210 μm thick plastic base, resulting in a total thickness of 350 μm. A nuclear emulsion comprises a large number of small AgBr crystals, uniformly dispersed in gelatine. When a charged particle crosses the emulsion layer, a sequence of AgBr crystals is sensitized along its trajectory, producing a latent image. After a chemical development procedure, the latent images turn into a sequence of dark silver grains, which can be seen with an optical microscope [11]. The darkness of these grains depends on the ionization of the particle.

Nuclear emulsion films used in the 2019 FOOT measurements were produced by the Nagoya University (Japan) and Slavich Company[1] (Russia) (75% and 25%, respectively). Their sensitivity corresponds to 30 grains over a track length of 100 μm for a minimum ionizing particle (MIP).

From the moment they are produced and until their chemical development, nuclear emulsion films are sensitive to charged particles. In particular, during their lifetime, they integrate all particle tracks from cosmic rays

---

1 https://www.slavich.com/

and environmental radioactivity. To avoid an unwanted background, before the detector assembly, films were transported in a random order, so that cosmic rays accumulated during that period have a different alignment and cannot be reconstructed as penetrating tracks. Nevertheless, they can still contribute to the background in case of random association of two or more aligned base-tracks.

2.2 Emulsion spectrometer exposure

The emulsion spectrometer was installed in cave A of the GSI facility. The incident beam flux was monitored by the start counter, made of a thin plastic scintillator, and by the beam monitor, consisting of a drift chamber that provides the beam spatial distribution.

The integrated flux in emulsion films was set at about 1,000 ^{16}O ions/cm^2, a trade-off between the need to avoid the pile-up of interactions in emulsions and the requirement for large statistics. The corresponding number of triggered events in the start counter was 19,375. The beam had a Gaussian shape (~1 mm sigma), a fixed energy, and was used to scan a square area of 2.4 cm side (in a grid of 25 × 25 points), starting from the center and following a squared spiral shape with 1 mm pitch.

2.3 Emulsion spectrometer structure

The emulsion spectrometer structure, shown in Figure 2, was built according to the emulsion cloud chamber (ECC) technique [12], which consists of nuclear emulsion films alternated with passive material layers. The emulsion
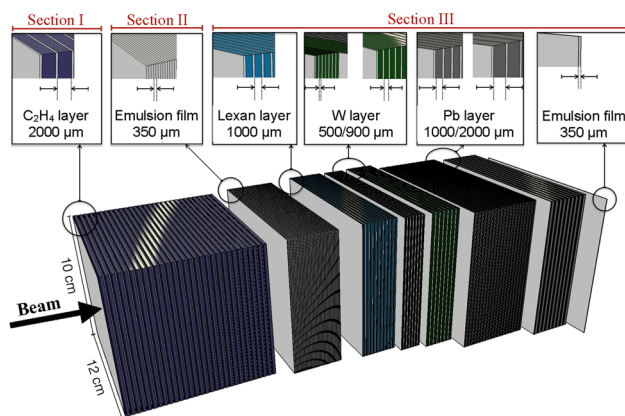

Figure 2: Structure of the emulsion spectrometer.

spectrometer structure is organized in three main sections: Section I acts as target region and vertex determination, Section II for the charge identification, and Section III for the momentum measurement and, consequently, isotopic identification of fragments.

Section I consists of 30 emulsion films interleaved with 30 polyethylene layers (2 mm thick) and is meant for the detection of beam interactions with the target (vertex detector). Its length is optimized so that about 33% of 200 MeV/n ^{16}O ions interacts therein, according to Monte Carlo simulations based on FLUKA code [13,14]. At this energy, the Bragg peak is contained in this section and occurs after 26 layers.

Section II is made of a sequence of 36 emulsion films divided into nine cells, each consisting of four films. The four nuclear emulsions of each cell underwent an appropriate thermal treatment to extend the dynamic range of the emulsion sensitivity to ionization with the aim of measuring the charge of fragments. A detailed description of the thermal process is reported later.

Section III is made of a sequence of 55 nuclear emulsion films interleaved with lexan (C$_{16}$H$_{14}$O$_3$, 1.2 g/cm^3, 1 mm thick), tungsten (19.25 g/cm^3, 0.5 mm, and 0.9 mm thick) and lead (11.34 g/cm^3, 1 mm, and 2 mm thick) layers. It is designed to measure particle momenta taking into account the particle range and the multiple Coulomb scattering (MCS) [15].

2.4 Track reconstruction

Emulsion films were analyzed by fast-automated microscopes with high tracking efficiency (~90%) and speed (up to 190 cm^2/h) [16–18]. The automated scanning system consists of a microscope equipped with a 3D motorized translation stage, a dedicated optical system and a CCD camera.

During the scanning, silver grains produced by the particle are recognized as aligned clusters of dark pixels and associated to form the so-called *micro track* in the emulsion layer, as shown in Figure 3. For each film, micro tracks on the top and bottom layers are then connected across the plastic base to form a *base-track*, with an accuracy of about 0.3 µm in position and 1.2 mrad in angle. A sequence of base-tracks in different emulsion films allows to reconstruct the particle trajectory inside the detector called *track* [19].

The sum of all pixels corresponding to the same track is proportional to the specific ionization of the incident particle.
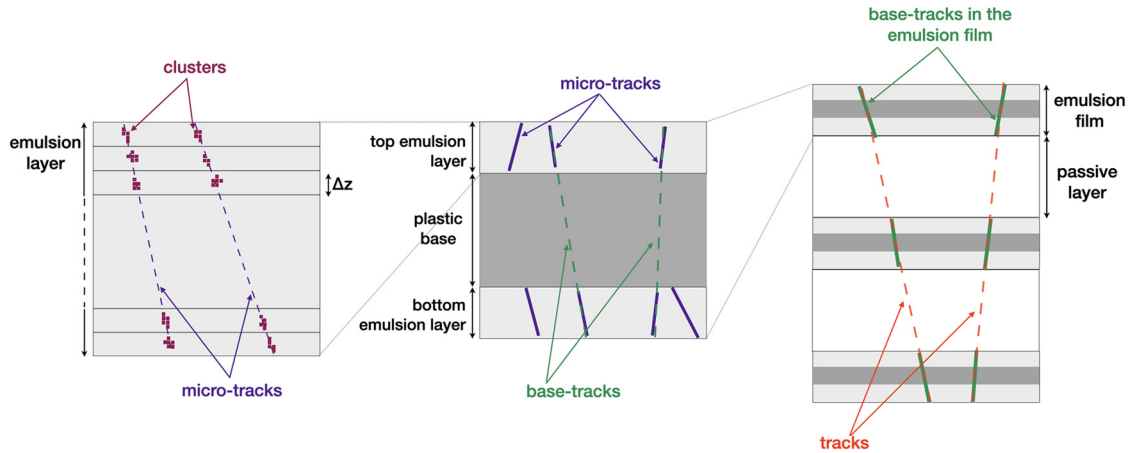
Figure 3: Schematic drawing of a micro-tracks reconstruction in different tomographic images, grabbed at equally spaced depth levels through the sensitive layer (left), micro-tracks association between two emulsion layers to form a base-tracks (center) and base-tracks association to form a track.

3 Charge identification

In nuclear emulsions, the grain density along particle trajectories is proportional to the particle energy loss over a certain dynamic range. For highly ionizing particles, such as the ion beam considered here and induced fragments, a saturation effect occurs due to the limited range of the grain density, thus preventing the charge measurement.

The dynamic range of the emulsion film response can be extended by keeping them for a certain amount of time, typically 24 h, at temperatures above 28°C with a relative humidity around 95%: a controlled fading is induced, which can partially or totally erase base-tracks of less ionizing particles [10]. The use of films that underwent different thermal treatments allows to recover the original ionization of the track, thus reconstructing the particle charge.

To exploit this technique, Section II was divided into nine cells of four emulsion films each, denoted as Rx, with $x \in \{0, 1, 2, 3\}$. Each of these films underwent a specific thermal treatment (see Figure 4): $R0$ films did not undergo any treatment, $R1$, $R2$, and $R3$ ones were kept for 24 h at 95% relative humidity and at a temperature of 28°C, 34°C, and 36°C, respectively. Applying these thermal treatments, the number of residual grains along the track will be progressively reduced, according to their ionization. For example, the erased fraction of base-tracks for cosmic rays has been measured to be larger than 99% in $R1$, while proton base-tracks are erased with an efficiency larger than 96% in $R2$.

For this analysis, Section II has been considered as a stand-alone detector. In Section II, 91,876 tracks were reconstructed. For each track, the following variables were evaluated:
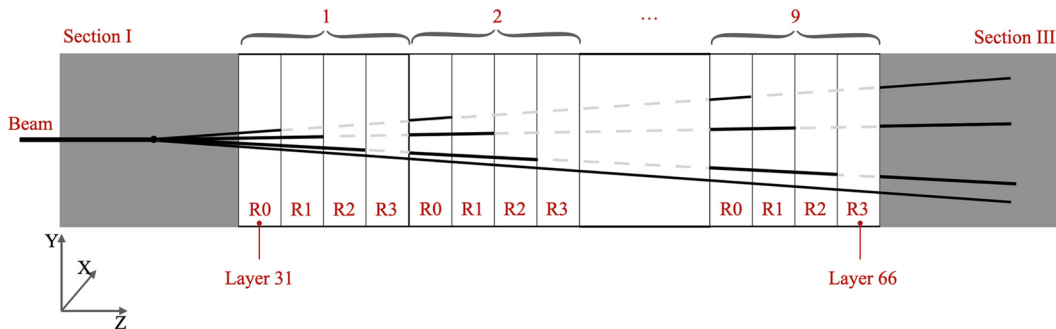

Figure 4: Section II is divided into nine cells, each one consisting of four emulsion films that underwent different thermal treatments. The more base-tracks survive to thermal treatments, the higher the particle's Z.

- $\tan\theta$: the tangent of the inclination of most upstream fitted track segment w.r.t. the Z-axis;
- NRx: the number of base-tracks belonging to the track for each set of thermal treatments Rx, with $x \in \{0, 1, 2, 3\}$;
- VRx: for each base-track, a variable named "volume" is defined as the sum of the pixel brightness and expressed in arbitrary units related to particles' ionization;
- $\langle VRx \rangle = \frac{\sum_{NRx} VRx}{NRx}$.

Combining these variables, the particle charge can be distinguished with two complementary methods: an analysis based on event selections, hereafter referred to as cut-based (CB) analysis, for MIP cosmic rays and $Z \leq 2$, and the principal components analysis (PCA) [20] for $Z \geq 2$ fragments. Excluding the combinatorial background, the sample can be divided into three disjoint sets, according to the number of base-tracks (NRx) survived to each thermal treatment.

Minimum ionizing particle tracks, such as muon cosmic rays, are expected to be erased from all thermal treatments; therefore, they are present only in $R0$ films. The same happens for high energy (≥ 80 MeV) protons, as shown in previous tests [9]. Nevertheless, given intrinsic statistical fluctuations of the number of grains, distributed according to a Poisson function, and thermal treatments efficiency, a single base-track may be formed in films other than $R0$. Therefore, the criterion adopted for the identification of these particles requires the reconstruction of track segments in $R0$ films and allows the presence of one track segment elsewhere: $NR0 > 1$ and $NRx_{x \in \{1,2,3\}} \leq 1$. The number of tracks fulfiling this request is 78,905, and MIP cosmic rays and high energy protons can be separated through a cut-based analysis.

The cut based-analysis is applied also to fragments surviving $R1$ thermal treatment ($NR0 > 1$ and $NR1 > 1$) that do not have a statistically significant number of base-tracks in $R2$ and $R3$ ($NR2 \leq 1$ and $NR3 \leq 1$) are 3,858.

Fragments not included in previous selections, whose base-tracks survived also to $R2$ and/or $R3$ thermal treatments, are 9,113, but for the PCA analysis, the presence of at least three $VRx_{x \in \{0,1,2,3\}}$ is required. This condition is satisfied by 7,529 fragments. The remaining tracks, about 1.7% of the whole sample (1,584), are due to the combinatorial background, which is formed by random association of spare base-tracks: 95% of these tracks, indeed, have less than four base-tracks without any specific correlation with Rx. As an example, if a track has three base-tracks, two of them in $R3$ and one in $R1$, this must be due to a random association of base-tracks, since it is not possible that a track has survived $R3$ thermal treatment without leaving any base-track in $R0$ and $R2$.

3.1 Identification of cosmic rays

First of all, we want to separate MIP cosmic rays from high energy (≥ 80 MeV) protons, which are particles that are expected to be erased from all thermal treatments.

From the $\langle VR0 \rangle$ profile, shown in Figure 5(a) for all particles fulfiling the request $NR0 \geq 0$ and $NRx_{x \in \{1,2,3\}} \leq 1$, it is possible to distinguish between two populations. These are well separated looking at $\tan\theta$, as in Figure 5(b). The particles at lower $\langle VR0 \rangle$ have angles which span over a wide range, mainly $\tan\theta > 0.4$. This behavior is expected for cosmic rays integrated during all the detector lifetime. Indeed, the beam direction is orthogonal to the emulsion film surface and fragments produced by beam interactions are expected at smaller angles w.r.t. the beam direction, while cosmic rays impinge at wider angles. The distribution is truncated at $\tan\theta = 1$ due to limits used during data reconstruction.
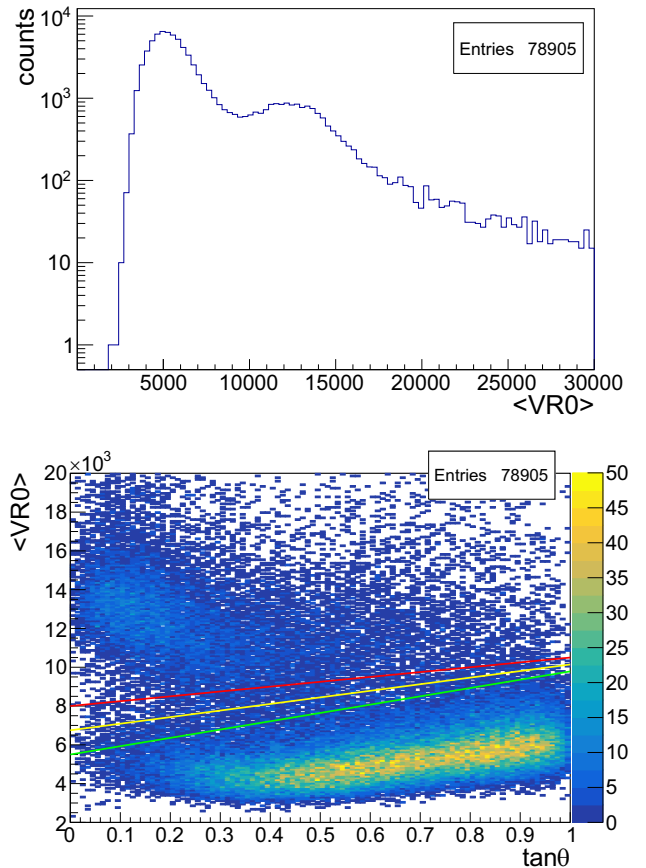

Figure 5: MIP particles ($NR0 \geq 0$ and $NRx_{x \in \{1,2,3\}} \leq 1$): (a) distribution of $\langle VR0 \rangle$ and (b) distribution of $\langle VR0 \rangle$ versus the track's angle $\tan\theta$. The yellow line represents the cut used to distinguish $Z = 1$ fragments (above the cut) by cosmic rays (below the cut). Green and red lines define the range of the boundary between the two populations.
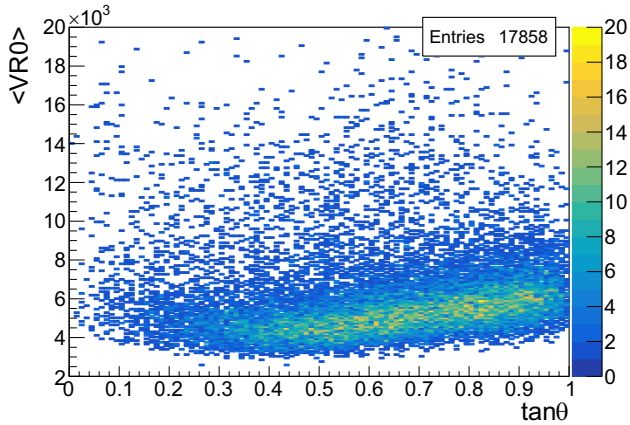
Figure 6: Results of a control sample exposed only to cosmic rays.

To study the behavior of cosmic rays, a control sample has been taken in a region of the emulsion spectrometer outside the signal area, where only cosmic rays are present. The distribution of $\langle VR0 \rangle$ versus $\tan \theta$ for these tracks is shown in Figure 6. These are mainly MIPs ($\langle VR0 \rangle \lesssim 8{,}000$), with a small component due to cosmic ray protons ($\langle VR0 \rangle \gtrsim 8{,}000$), as expected by cosmic rays flux measurements [21].

Therefore, MIP cosmic rays can be identified by combining the information of NRx, $\tan \theta$, and $\langle VR0 \rangle$. The yellow line in Figure 5 is used to separate in the plane ($\langle VR0 \rangle$, $\tan \theta$) cosmic rays and $Z = 1$ fragments, which have higher ionization. Green and red lines, instead, define the range of the boundary between the two populations and therefore have been used to evaluate the systematic uncertainty, given by half of the difference between the highest and lowest values obtained.

With this analysis condition, 60,126 particles out of 78,905 are identified as MIP cosmic rays and 18,779 as $Z = 1$ fragments. The systematic uncertainty due to the selection is estimated to be 3% for cosmic rays and 8% for $Z = 1$ fragments.

At this stage, only the charge is measured, while the isotopic discrimination task is addressed in Section III; therefore, we refer to these fragments as $Z = 1$ rather than protons. The same will apply to $Z > 1$ fragments.

3.2 Identification of $Z \leq 2$ fragments with a cut-based analysis

There are 3,858 fragments that have not been included in previous selection because of $NR1 > 1$ and that do not have a statistically significant number of base-tracks in

$R2$ and $R3$ ($NR2 \leq 1$ and $NR3 \leq 1$). These are shown in Figure 7, where the $\langle VR1 \rangle$ is plotted versus $\langle VR0 \rangle$. One population is visible: tracks with $\langle VR1 \rangle$ below the yellow line in Figure 7 are due to $Z = 1$ fragments, but more ionizing than the ones already identified having $NR1 \leq 1$. At equal charge, higher ionization corresponds to lower energy, so these tracks are identified as due to lower energy $Z = 1$ fragments. Light blue and magenta lines define possible choices in the definition of the boundary to select this population and therefore were used to evaluate systematic uncertainties.

Fragments with $\langle VR1 \rangle$ larger than the cut have been interpreted as belonging to the next atomic species, $Z = 2$.

The hypothesis of two populations and their boundaries are confirmed by the same plot without any cut applied on $NR2$ and $NR3$, as shown in Figure 8. The number of fragments below the straight line is almost stable in the two cases, demonstrating that those are $Z = 1$ particles which do not survive thermal treatments more aggressive than $R1$. On the contrary, tracks above the straight line show higher ionization and are thus fragments with $Z \geq 2$. When $NR2$ and $NR3$ are missing, the higher energy component with Z equal to 2 is selected. Most of the tracks with $Z \geq 2$ will be analyzed in the next section with the PCA analysis.

From the information retrieved from $R0$ and $R1$ films, the charge has been measured for 3,858 particles: 2,420 fragments constitute the $Z = 1$ populations, while 1,438 have been recognized as $Z = 2$ fragments. The systematic uncertainty due to the selection is estimated to be 8% for $Z = 1$ and 11% for $Z = 2$.
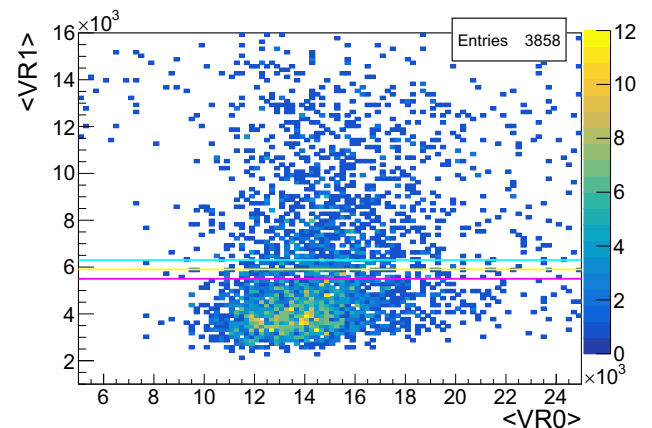

Figure 7: Distribution of $\langle VR1 \rangle$ versus $\langle VR0 \rangle$ for tracks with $NR2 \leq 1$ and $NR3 \leq 1$. The yellow line represents the cut used to distinguish high energy $Z = 2$ fragments (above the cut) by low energy $Z = 1$ ones (below the cut). Magenta and light blue lines define the range of the boundary between the two populations.
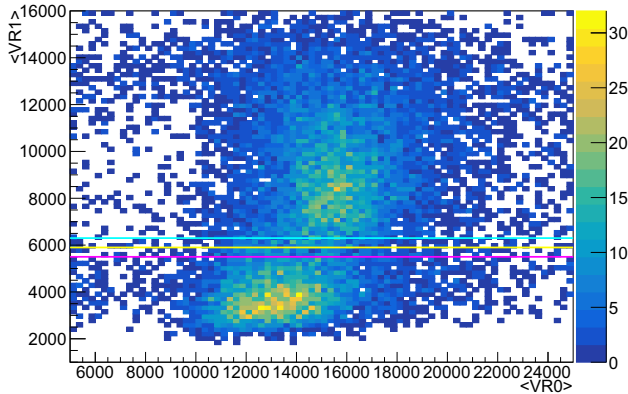
Figure 8: Distribution of $\langle VR1 \rangle$ versus $\langle VR0 \rangle$ for all tracks with $NR1 > 1$. No cuts have been applied on $NR2$ and $NR3$. The yellow line separates $Z \geq 2$ fragments (above) by low energy $Z = 1$ ones (below). Magenta and light blue lines define the range of the boundary between the two populations.

Excluding cosmic rays from the sample, with the cut-based analysis, the charge has been measured for 74% of fragments. A summary of the charge measured is reported in Table 1. The $\tan \theta$ distribution for cosmic rays is reported in Figure 9, compared with the distribution

of other fragments whose charge was measured with the cut-based analysis.

3.3 Identification of $Z \geq 2$ fragments with the principal component analysis

To further distinguish $Z \geq 2$ fragments surviving also $R2$ and/or $R3$ thermal treatments, a cut-based analysis on $\langle VR2 \rangle$ and $\langle VR3 \rangle$ variables is not powerful enough due to saturation effects, as shown in Figure 10, where only cuts $\langle VR2 \rangle > 0$ and $\langle VR3 \rangle > 0$ were applied.

In order to disentangle different fragment tracks, the principal component analysis, a multidimensional technique, well established in the field of pattern recognition [20] was adopted. This technique is based on applying a linear transformation to the measured variables and is useful when these are not the most significant for data classification, while reducing the dimensionality of the problem results in an easier classification procedure.
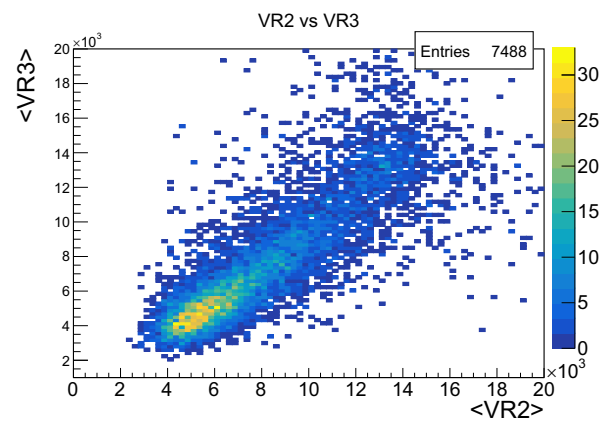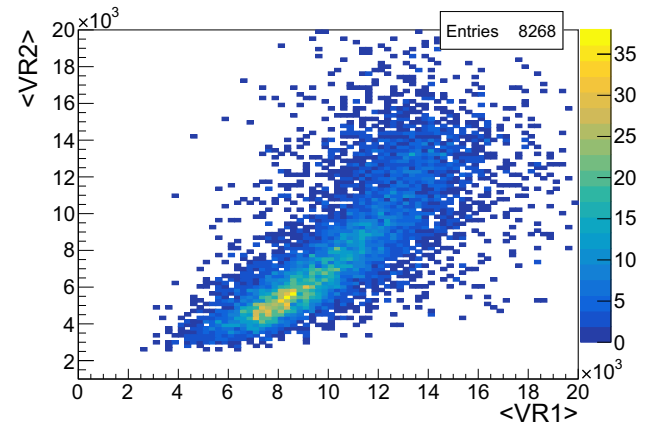
Table 1: Number of fragments classified as $Z = 1$ or high energy $Z = 2$ with the cut-based analysis

Z	Number of tracks	Syst. Err.
1	21,199	1,649
2 (high energy)	1,438	161
Measured	22,637	

Figure 9: Distribution of the inclination of cosmic rays and of fragments identified by the cut-based analysis.

Figure 10: Tracks volume distribution for $\langle VR2 \rangle$ vs $\langle VR1 \rangle$ (top) and $\langle VR3 \rangle$ vs $\langle VR2 \rangle$ (bottom) variables.

This transformation, described by an orthogonal matrix, is equivalent to a rotation of the original pattern space into a new set of coordinate vectors.

Being **V R**, the vector containing our measured values, the covariance matrix is defined as $\mathbf{C} = \langle \mathbf{yy^T} \rangle$, where $\mathbf{y} = \mathbf{V\,R} - \langle \mathbf{V\,R} \rangle$. **C** matrix is real, positive definite, symmetric, and with non-null, positive eigenvalues.

The base formed by the eigenvectors of the **C** matrix and belonging to the largest eigenvalues corresponds to the most significant features of the description of the original prototypes.

The PCA method was applied to all fragments with at least three measured VRx, which are 7,529. For these fragments, four new variables called VP_{xyz} are defined. These variables are expressed in arbitrary units as VRx.

The first principal component is calculated to account for the highest variance in the data.

Considering how VP_{xyz} have been evaluated, particles with higher ionization are expected to also have a higher VP_{xyz}.

Each of these variables was fitted with three Gaussian functions, as shown in Figure 11. To each Gaussian fit, the particle population with increasing Z was associated: violet for $Z = 2$ fragments, pink for $Z = 3$, and green for $Z \geq 4$ ones. The fit model has been inferred by the study of a high-purity sample requiring tracks crossing at least 7 cells ($NR0 \geq 7$). With the cut-based analysis, a fraction of $Z = 2$ fragments was already identified. Therefore, in the complementary sample, which survived after the more aggressive thermal treatment applied on $R2$ and $R3$, the component of $Z = 2$ fragments with higher ionization (lower energy) is expected. For this reason, the $Z = 2$ Gaussian will be partially erased. The threshold value depends on the particle energy and on the statistical fluctuation in the number of sensitized grains along the track. These effects produced a smearing in the threshold that is not expected to be sharp. Therefore, the fit is not taking into account low VP_{xyz} values, where the behavior is not Gaussian. Another requirement is that the height of $Z = 2$ Gaussian peak must be higher than that of the $Z = 3$ Gaussian, which in turn has to be higher than or equal to the height of the $Z \geq 4$ Gaussian, since the number of fragments is expected to decrease as Z increases. Consequently, the mean value of the $Z = 2$ Gaussian is lower than the mean value of $Z = 3$ Gaussian, which in turn is lower than the mean value of $Z \geq 4$ Gaussian.

The charge is assigned to each fragment by generating a random number which takes into account probabilities given by the height of each Gaussian curve for its VP_{xyz} value with respect to the height of the overall fit
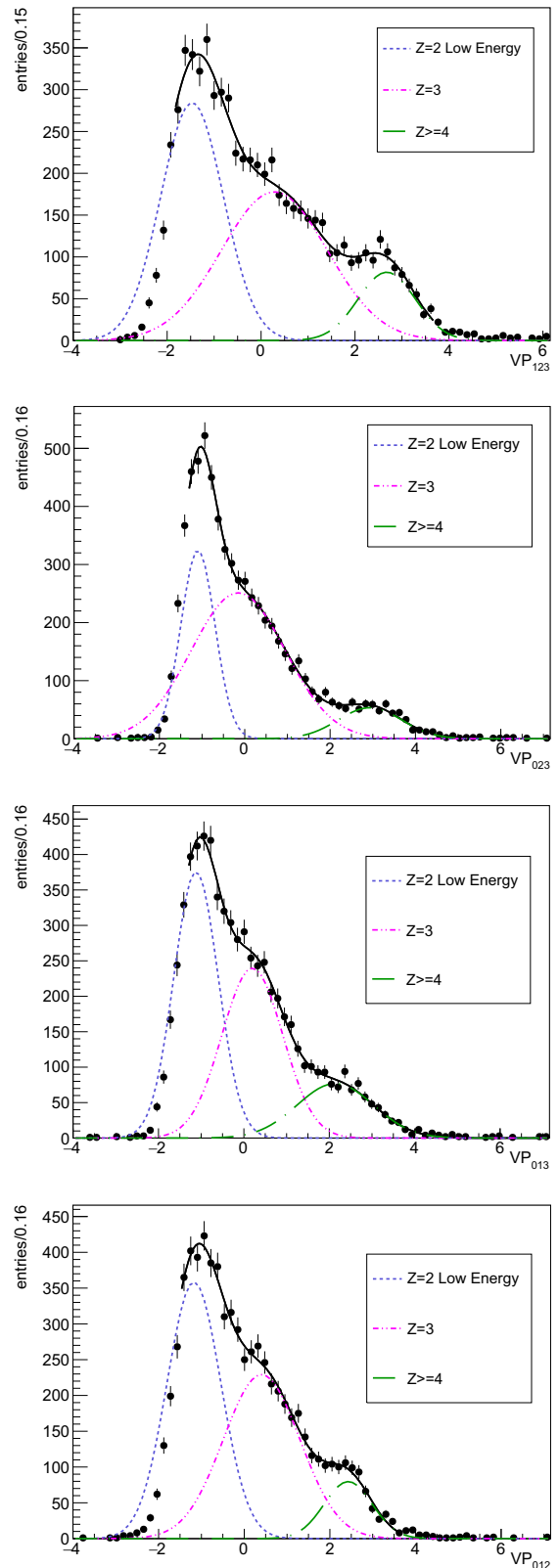

Figure 11: Distributions of the four variables obtained with the PCA method: black dots represent data. Each Gaussian fit corresponds to a particle Z: violet for $Z = 2$ fragments, pink for $Z = 3$, and green for $Z \geq 4$.

distribution. As far as the evaluation of the relative contribution of each population is concerned, this method is equivalent to estimating the relative weight of each Gaussian distribution. Nevertheless, the procedure outlined above is meant to provide an additional feature to each track that could be useful for future analysis.

The variable VP_{123} is used if $\langle VR1 \rangle$, $\langle VR2 \rangle$, and $\langle VR3 \rangle$ are available. Especially for tracks with a small number of segments, it can happen that segments in a specific Rx are not reconstructed or are not correctly associated with the track, so it is not possible to evaluate their VRx. In this case, one of the other VP_{xyz} combinations applies. In Table 2, we report the number of fragments tagged with the corresponding variable.

Three error components have been identified: a systematic uncertainty due to the fit, which can differ because of plot binning or lower limit, the error due to uncertainties of the fit parameters and a statistical error due to the size of the available sample. All error components have been evaluated only for VP_{123}: the contribution of the error coming from the other VP_{xyz}, indeed, is negligible with respect to the one of VP_{123}, which is used for more than 90% of fragments.

To evaluate the systematic uncertainty, six fits have been applied, which differ from each other for the plot binning and lower limits. For each one of them, the error due to uncertainties of fit parameters was evaluated through the generation of 10^4 fits, where mean values of the three Gaussian curves are normally distributed around their mean within 1σ. Only fits with a probability larger than 0.001 have been accepted. An example is shown in Figure 12.

For each of the six different fits, the average on the results obtained over the 10^4 random generations gives a partial estimation of the number of particles with a given Z. The final result is obtained as the weighted average on these six partial results. The systematic uncertainty is given by the maximum error on the six results, while the statistical error is given by the standard deviation
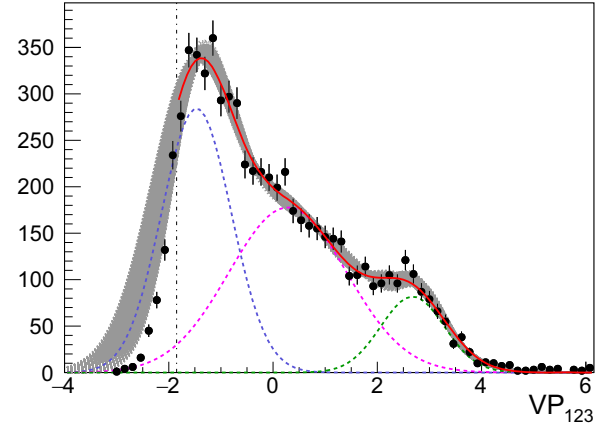

Figure 12: Example of 10^4 fits (in gray) generated within uncertainties of fit parameters.

on the weighted average. The main contribution is due to the systematic uncertainty, while the statistical error and the one due to uncertainties of fit parameters are negligible.

The number of fragments for each Z is reported in Table 3, together with relative uncertainties. Combining the $\langle VRx \rangle$ information through the PCA, the charge has been assigned also to fragments with $Z \geq 2$. It is not possible to further distinguish $Z \geq 4$ particles with the current thermal treatments used.

To crosscheck the results obtained with PCA, other two methods have been tried: the singular value decomposition (SVD) and the non-negative matrix factorization (NMF) [22]. Both lead to compatible results within the errors.

3.4 Results

The charge has been measured or assigned for 98.3% of reconstructed particles. Different fragments identified and corresponding fractions are reported in Table 4.
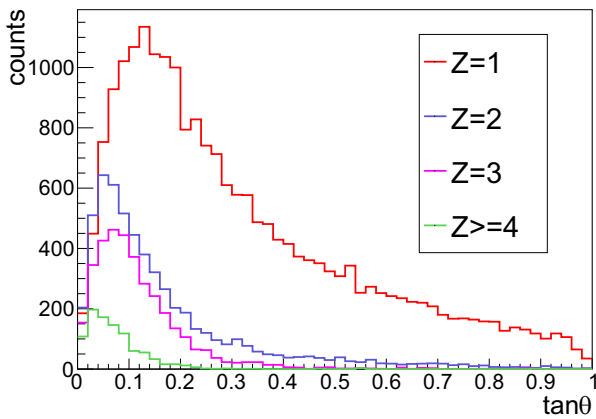
The $\tan\theta$ distribution for all identified fragments is shown in Figure 13. The mean and RMS of distributions

Table 2: Number of fragments classified with the PCA method and the corresponding variable. If available, VP_{123} is preferred, otherwise one of the other VP_{xyz} is used, according to which $\langle VRx \rangle$ have been evaluated

VP_{xyz}	Number of tracks	%
VP_{123}	6,801	90.3
VP_{012}	546	7.3
VP_{013}	111	1.5
VP_{023}	71	0.9

Table 3: Number of fragments classified as low energy $Z = 2$, $Z = 3$ and $Z \geq 4$ with PCA method

Z	Number of tracks	Syst. Err.
2 (low energy)	3,506	370
3	2,915	560
≥4	1,108	300
Assigned	7,529	

Table 4: Percentage of fragments classified for each Z, excluding cosmic rays

Z	Fragments classification					
	CB	PCA	Total	%	Syst. Err. (%)	Stat. Err. (%)
1	21,199	/	21,199	70	5	0.7
2	1,438	3,506	4,943	16	2	1.4
3	/	2,915	2,915	10	2	1.9
≥4	/	1,108	1,108	4	1	3.0
Total	22,637	7,529	30,166			

Figure 13: Distribution of inclination for fragments with $\tan\theta < 1$.

Table 5: Mean and RMS of fragments inclination distributions, referred to Figure 13

Z	$\langle tan\,\theta \rangle$	RMS
1	0.32	0.23
2	0.17	0.17
3	0.11	0.09
≥4	0.08	0.07

are reported in Table 5. As expected, the mean of the distributions decreases with increasing Z.

4 Conclusion

In this study, the charge identification of fragments produced in interactions of 200 MeV/n oxygen ions with a C_2H_4 target has been reported. Thermal treatments inducing controlled fading of nuclear emulsion films were applied to the Section II of the emulsion spectrometer to distinguish the charge of fragments generated by oxygen interactions and separate them from cosmic rays integrated during the detector lifetime. The charge was measured or assigned for 99.4% of tracks reconstructed in Section II of the detector. The charge of these fragments was measured using two complementary methods: a cut-based analysis and the principal component analysis. Our aim was to identify fragments as heavy as lithium, and this goal was achieved. Within the FOOT experiment, identification of $Z \geq 4$ fragments is a task of the electronic detector setup. For future data takings, the systematic uncertainty, which is the dominant one, will be reduced by optimizing the thermal treatments to get a better separation between fragments with different charge.

References

[1] Paganetti H, Niemierko A, Ancukiewicz M, Gerweck LE, Goitein M, Loeffler JS, et al. Relative biological effectiveness (RBE) values for proton beam therapy. Int J Radiation Oncology Biol Phys. 2002;53(2):407–21.

[2] Tommasino F and Durante M. Proton radiobiology. Cancers. 2015;7:353–81.

[3] Durante M, Paganetti H. Nuclear physics in particle therapy: a review. Rep Prog Phys. 2016;79:096702.

[4] Paganetti H. Relative Biological Effectiveness (RBE) values for proton beam therapy. Variations as a function of biological end-point, dose, and linear energy transfer. Phys Med Biol. 2014;59(22):R419.

[5] De Lellis G, Buontempo S, Di Capua F, Di Crescenzo A, Migliozzi P, Petukhov Y, et al. Measurements of the fragmentation of carbon nuclei used in hadron therapy. Nucl Phys A. 2011;853:124–34.

[6] G. Battistoni, Toppi Marco, Patera V, (FOOT collaboration). Measuring the impact of nuclear interaction in particle therapy and in radio protection in space: the foot experiment. Front Phys. 2021. doi: 10.3389/fphy.2020.568242.

[7] https://web.infn.it/f00t/index.php/it/public links. 2020.

[8] De Lellis G, Buontempo S, Di Capua F, Marotta A, Migliozzi P, Petukhov Y, et al. Emulsion Cloud Chamber technique to measure the fragmentation of high-energy carbon beam. J Instrum. 2007;2:P06004.

[9] Montesi MC, Lauria A, Alexandrov A, Alunni Solestizi L, Giovanni A, Argiró S, et al. (FIRST Collaboration). Ion charge separation with new generation of nuclear emulsion films. Open Phys. 2019;17(1):233–40.

[10] Nakamura T, Ariga A, Ban T, Fukuda T, Fukuda T, Fujioka T, et al. The OPERA film: new nuclear emulsion for large-scale, high-precision experiments. NIMA-A. 2006;556:80–6.

[11] A Ariga, T Ariga, G De Lellis, A Ereditato, K Niwa. Nuclear emulsions. Cham: Springer International Publishing; 2020. p. 383–438.

[12] De Lellis G, Buontempo S, Di Capua F, Marotta A, Migliozzi P, Petukhov Y, et al. Emulsion cloud chamber technique to measure the fragmentation of a high-energy carbon beam. JINST. 2007;2:P06004.

[13] Battistoni G, Bauer J, Boehlen T, Cerutti F, Chin M, Santos Augusto R, et al. The FLUKA code: An accurate simulation tool for particle therapy. Front Oncol. May 2016;6:116. doi: 10.3389/fonc.2016.00116.

[14] Ferrari A, Sala PR, Milan/CERN/INFN, Fasso A, /SLAC, Ranft J, Siegen U. FLUKA: A multi-particle transport code. 12 2005.

[15] Agafonova N, Aleksandrov A, Altinok O, Anokhina A, Aoki S, Ariga A, et al. Momentum measurement by the multiple Coulomb scattering method in the OPERA lead emulsion target. New J Phys. 2012;14:013026.

[16] Alexandrov A, Buonaura A, Consiglio L, D'Ambrosio N, De Lellis G, Di Crescenzo A, et al. A new fast scanning system for the measurement of large angle tracks in nuclear emulsions. J Instrum. 2015;10:P11006.

[17] Alexandrov A, Buonaura A, Consiglio L, D'Ambrosio N, De Lellis G, Di Crescenzo A, et al. A new generation scanning system for the high-speed analysis of nuclear emulsions. J Instrum. 2016;11:P06002.

[18] Alexandrov A, Buonaura A, Consiglio L, D'Ambrosio N, De Lellis G, Di Crescenzo A, et al. The continuous motion technique for a new generation of scanning systems. Sci Rep. 2017;7(1):7310.

[19] Aleksandrov A, Consiglio L, De Lellis G, Di Crescenzo A, Lauria A, Montesi MC, et al. Measurement of large angle fragments induced by 400 MeV $n-1$ carbon ion beams. Meas Sci Technol. 2015;26(9):094001.

[20] CERN-72-21. 1972 CERN Computing and Data Processing School, Pertisau, Austria, 10-24 Sep 1972: Proceedings, CERN Yellow Reports: School Proceedings, 12 1972. https://cds.cern.ch/record/186411.

[21] Grieder PKF. Cosmic rays at Earth. Amsterdam: Elsevier Science; 2001.

[22] Eldén L. Numerical linear algebra in data mining. Acta Numerica. May 2006;15:327–84.